Journal of Materials Chemistry A

ROYAL SOCIETY OF CHEMISTRY

PAPER

View Article Online
View Journal | View Issue

Cite this: J. Mater. Chem. A, 2024, 12, 28149

Ultrafast flash joule heating synthesis of the Pt/MoO_x heterostructure for enhancing the electrocatalytic hydrogen evolution reaction†

Lijuan Zhu,[a] Zhongjie Lai,[a] Jilong Xu,[a] Peiyu Ma,[a] Jiaxiang Lu,[a] Qian Xu,[a] Yitao Lin,[b] Lei Zheng,[c] Lihui Wu,[a] Honghe Ding,*[a] Jiawei Ge*[d] and Yifan Ye *[a]

The metal–support interaction of heterogeneous catalysts has garnered significant attention due to its role in boosting electrocatalytic efficiency. Herein, we synthesized uniformly dispersed Pt nanoparticles decorated on a MoO_x support by an ultrafast flash joule heating method. This method enables the simultaneous loading of metal and modification of support structures in a controllable, ultrafast manner. The optimal catalyst demonstrates exceptional performance in the hydrogen evolution reaction (HER) under acidic conditions, characterized by a low overpotential of only 55.08 mV to achieve a current density of 100 mA cm^{-2}, a Tafel slope of 19.94 mV dec^{-1}, and a significant mass activity of 13.80 A mg_{Pt}^{-1} at 50 mV *vs.* RHE. In addition, the optimal catalyst exhibits better stability for the HER than a commercial 20 wt% Pt/C catalyst. The spectroscopic characterization confirms the charge transfer between the metal and support, leading to a near-zero valence state of Pt in the optimal catalyst. Density functional theory calculations further corroborate that the metal–support interaction between Pt and MoO_x leads to a suitable hydrogen adsorption free energy at the interfacial Pt site, which results in accelerating the reaction kinetics of the HER. This work aims to design and develop a metal–support heterostructure with high HER activity and stability, and provides a strategy for engineering crystalline structures and electronic configurations using an ultrafast flash Joule heating synthesis method.

Received 22nd July 2024
Accepted 10th September 2024

DOI: 10.1039/d4ta05081a

rsc.li/materials-a

Introduction

To tackle global warming and reduce carbon emissions, shifting our energy source from fossil fuels to renewable energy is crucial. Hydrogen energy, recognized as a clean energy source with eco-friendliness, sustainability, and high calorific value, is considered one of the most promising alternatives to traditional fossil fuels.[1–3] As an efficient approach for converting energy into the chemical energy stored in clean energy H_2, the electrochemical hydrogen evolution reaction (HER) has drawn much attention for its green production process.[4,5] Electrocatalysts are pivotal in the HER, where they serve to lower the overpotential and enhance hydrogen production efficiency.[6,7] Thus, it is highly imperative to develop affordable but efficient electrocatalysts to meet the rapidly escalating demand for HER catalysis.

The state-of-the-art platinum (Pt) electrocatalysts have exhibited outstanding catalytic activity and fast kinetics toward the HER because of their low hydrogen absorption Gibbs free energies (ΔG_{H^*}).[8,9] However, it is difficult to widely produce Pt-based electrocatalysts due to their scarcity and high costl.[10] Hence, the quest to design highly efficient electrocatalysts that minimize Pt usage while preserving their outstanding activity is imminent. Abundant research has demonstrated that modulation by metal–support interactions can be a promising strategy to tune catalytic performance efficiently.[8,9,11,12] Wang and co-workers successfully prepared Pt_{SA}/α-MoC_{1-x}@C with a unique electronic structure because of metal–support interaction, which showed an exceptional performance for the HER.[13] In addition, Shan and her team[14] utilized the 2H–MoS_2 support to regulate the electrical structure of interfacial Pt sites, which largely enhanced HER activity. Therefore, exploiting a suitable support to modulate the electronic structure of Pt sites is crucial for achieving enhanced HER catalytic performances.

Transition metal oxides are commonly employed as supports for noble metals to modulate catalyst active sites.[15–18] Among these transition metal oxides, molybdenum trioxide (MoO_3) has a layered structure, which is conducive to the removal/insertion of small ions such as H^+, but its low electrical conductivity and the lack of sufficient active sites in MoO_3 makes it show poor catalytic performance for the HER.[19–22] Fortunately, despite the

[a]National Synchrotron Radiation Laboratory, University of Science and Technology of China, Hefei 230029, PR China. E-mail: yifanye92@ustc.edu.cn
[b]Department of Engineering Physics, Tsinghua University, Beijing 100084, PR China
[c]Institute of High Energy Physics Chinese Academy of Sciences, Beijing 100049, PR China
[d]School of Chemistry and Materials Science, University of Science & Technology of China, Anhui 230026, China

† Electronic supplementary information (ESI) available. See DOI: https://doi.org/10.1039/d4ta05081a

poor catalytic performance of pure phase MoO_3, the formation of MoO_3 composites can effectively improve the catalytic performance.[21,23] Inspired by this, we hypothesize that anchoring Pt nanoparticles on a heterogeneous composite support (MoO_x) helps accelerate the reaction dynamics of the HER.

So far, some reports[9,24,25] have discussed the production and performance of Pt-based heterogeneous electrocatalysts. For instance, Dong and his team[23] prepared low-content Pt loading on the MoO_2/MoS_2 heterostructure ($Pt@MoO_2/MoS_2$) by hydrothermal and electrodeposition methods, which led to an exceptional performance for the hydrogen evolution reaction. In Park's research,[26] people used an annealing method to prepare a Pt_{SA}/WO_{3-x} catalyst for the HER, which exhibited equivalent HER performance to the benchmark catalyst due to the optimized chemical interactions between Pt atoms and the substrate. However, the above traditional preparation methods often suffer from complicated steps, lengthy processes, and high energy consumption. In contrast, the ultrafast joule heating method is gradually becoming one of the advanced methods for preparing nanocatalysts[27,28] due to its efficient and controllable characteristics.

The ultrafast flash joule heating (FJH) device works based on the Joule heating law $Q = U^2R^{-1}t$, where Q represents the generated heat, U indicates the voltage applied to the sample, R indicates the resistance, and t denotes the heating time.[27,29] The heating principle utilizes millisecond current pulses through the sample positioned between two conductive electrodes (Cu electrodes in this work), heating it to several thousand Kelvin and then cooling down rapidly to room temperature. The FJH method was first demonstrated for its unique capability in preparing a metastable alloy due to the rapid heating and cooling rate, which facilitates kinetic control over the thermodynamic mixing regimes and enables the formation of crystalline solid-solution nanoparticles.[28] Later, Deng and co-workers[29] confirmed the feasibility of preparing phase-controllable transition metal carbide nanocatalysts using the FJH method. However, there is still a lack of investigation using this rapid method to prepare metal–support nanocatalysts.

Considering that metal–metal oxide interfacial interaction helps to anchor metal on the support during the rapid heating process, it is feasible to prepare a Pt–support catalyst using this FJH method. In addition, although there are many current studies on Pt–support nanocatalysts,[9,14,24–26,30] the interaction between Pt and the heterogeneous support along with the HER mechanism has not been unveiled thoroughly. Therefore, we plan to systematically study the electron states and interfacial atomic configurations of our optimal catalyst through the combination of various spectroscopic techniques to uncover the structure–performance relationship for the Pt–support catalysts and further promote their applications in energy-related fields.

Herein, we prepared Pt nanoparticles loaded on the MoO_x support (Pt/MoO_x-F, F represents ultrafast flash joule heating method) as a highly efficient HER electrocatalyst by the FJH method. The X-ray diffraction and transmission electron microscopy measurements show that Pt nanoparticles are successfully loaded on the modified substrate. As a result, the Pt/MoO_x-F catalyst with an ultra-low Pt loading (1.853 wt%) has achieved superior activity for acidic HER. Moreover, X-ray absorption spectroscopy combined with X-ray photoelectron spectroscopy revealed that the Pt of Pt/MoO_x-F catalyst displays a valence state close to zero due to the strong electronic interaction between the support and Pt. Theoretical calculations further demonstrate that the metal–support interaction between Pt and the MoO_x substrate can effectively optimize the adsorption or desorption energy of intermediates. This work not only provides a design strategy to synthesize a heterogeneous Pt–support electrocatalyst but also reveals the mechanism of efficient catalysis of the HER from both theoretical and experimental aspects.

Experimental section

Materials and equipment

All the reagents were of analytic grade and used as purchased without further purification. Molybdenum dioxide (MoO_2, 99%), platinum black (Pt > 99.9%, metal basis), and $H_2PtCl_6 \cdot 6H_2O$ (chloroplatinic acid hexahydrate) were purchased from Aladdin Holdings Group Co., Ltd. Molybdenum trioxide (MoO_3, 99.5%) was purchased from Shanghai Huayi Huayuan Chemical Co., Ltd. Platinum on carbon (20%), ethanol (C_2H_5OH) and sulfuric acid (H_2SO_4, 98%) were purchased from Shanghai Macklin Biochemical Technology Co., Ltd. Nafion (5.0 wt%) was purchased from Shanghai Aladdin Biochemical Technology Co., Ltd. Carbon black (Cabot, VULCANXC72) was used as the carbon source. All aqueous solutions were prepared using deionized water with a resistivity of 18.2 MΩ cm^{-1}. An ultrafast flash joule heating device (CIS-JH3.2) was purchased from Hefei In situ Technology. Co., Ltd. By adjusting the voltage, temperatures from 600 °C to 2000 °C can be achieved.

Fabrication of electrocatalysts

The optimal catalyst Pt/MoO_x-F was synthesized by the ultrafast flash joule heating method. Initially, an appropriate amount of 10 mM H_2PtCl_6 solution was added to the MoO_3 powder at a molar ratio of Pt : Mo = 5 : 100 and then dried in an oven at 40 °C. The powder obtained after drying was mixed with carbon black by using a mortar and pestle in a mass ratio of 1 : 1 to obtain the Pt precursor. The precursor can be evenly mixed after long-term manual grinding (Fig. S1†). Subsequently, ~50 mg Pt precursor was placed in the joule heating device, and the temperature was adjusted to reach about 750 °C within 0.5 seconds at a controlled voltage of 20 V, and then rapidly reduced to room temperature. The obtained sample was named Pt/MoO_x-F, where F represents ultrafast flash joule heating. The value of "x" is approximately 2.4 and the specific calculation process for "x" can be found in the ESI (Table S1).†

The heterogeneous MoO_x support was synthesized by the same procedure as in the previous Pt/MoO_x-F step but without the addition of H_2PtCl_6 aqueous solution.

The Pt NPs catalyst was synthesized by the same procedure as in the previous Pt/MoO_x-F step, but without incorporating the MoO_3 powder (Fig. S2†).

The synthesis process of Pt/MoO_2 and Pt/MoO_3 was the same as that of Pt/MoO_x-F, except for the applied voltage. The applied voltages for Pt/MoO_3, Pt/MoO_x-F, and Pt/MoO_2 were 15 V, 20 V, and 22 V, respectively.

For the synthesis of Pt/MoO_x-P (P denotes a physical method), a straightforward physical mixing technique was employed. The mass ratio of the components in Pt/MoO_x-P is the same as that obtained from Pt/MoOx-F (Fig. S3 and Table S2†). The specific stages involved are detailed as follows: Pt black, MoO_3 and MoO_2 were measured out in a mass fraction ratio of 1.853 : 50 : 50. These components were then thoroughly ground together using a mortar and pestle for 30 minutes. The powder obtained from this process is referred to as Pt/MoO_x-P.

Characterization of the catalysts

The phase purity and crystal structure of the catalysts were determined by X-ray diffraction (XRD) at room temperature on a Mini-Flex 300/600 diffractometer with a voltage of 40 kV and a current of 15 mA. Transmission electron microscopy (TEM), high-resolution TEM (HR-TEM), and mapping images were captured using a JEOL-2100Plus with a 200 kV acceleration voltage. The X-ray photoelectron spectroscopy (XPS) measurements were performed at the Catalysis and Surface Science End station at the Beamline BL11U in the National Synchrotron Radiation Laboratory (NSRL, Hefei, P. R. China) with an excitation source of 380 eV and 600 eV. The ultraviolet photoelectron spectroscopy (UPS) measurements were also performed at the Beamline BL11U with an excitation source of 40 eV. The X-ray absorption fine structure (XAFS) measurements of the Pt L_3-edge and the Mo L_3-edge were performed at the beamline 1W1B station and beamline 4B7A station, Beijing Synchrotron Radiation Facility (BSRF), China, respectively.

Electrochemical measurements of the catalysts

All electrochemical measurements were performed by using an electrochemical workstation (CHI 760E) in N_2-saturated 0.5 M H_2SO_4 at room temperature. A three-electrode cell equipped with a graphite rod was used as the counter electrode, an Ag/AgCl electrode was used as the reference electrode, and the working electrode was fabricated by using each catalyst. The fabrication processes of the working electrode are as follows: 2.5 mg of each catalyst with 15 μL of 5 wt% Nafion solution was dispersed in 0.5 mL of a water/ethanol mixed solvent (1 : 3 volume ratio) followed by 30 min of sonication to form a homogeneous solution. Then, 5 μL of the above catalyst solution was dropped on the surface of a glassy carbon disk with a diameter of 3 mm (calculated catalyst loading: 342 μg cm^{-2}). To evaluate the activity of the catalysts, polarization curves were recorded at a sweep rate of 5 mV s^{-1}. The potentials were corrected to compensate for the effect of solution resistance, which were calculated by using the following equation: $E_{iR\text{-corrected}} = E(V\ vs.\ \text{RHE}) - iR$ and $E(V\ vs.\ \text{RHE}) = E(\text{Ag/AgCl}) + E(\text{Ag/AgCl})^0 + 0.0591\text{pH}$, where i is the current and R is the uncompensated ohmic electrolyte resistance. The mass activity was obtained by normalizing the current density to the Pt loading on the working electrode. Tafel slopes were calculated by fitting the linear portion of the polarization curves to the Tafel equation: $\eta = b \log j + c$, where η is the overpotential, b is the Tafel slope, j is the current density, and c is the intercept. Measurements of double-layer capacitance (C_{dl}) were made by scanning cyclic voltammetry (CV) at various scan rates from 20 to 120 mV s^{-1}. The durability test was conducted by multi-current steps (ISTEP) at 50 mA cm^{-2} for 15 h.

DFT calculation

The density functional theory (DFT) calculations were carried out based on the Vienna *Ab initio* Simulation Package (VASP). The Perdew–Burke–Ernzerhof (PBE) functional of the generalized gradient approximation (GGA) was employed with the projector augmented wave (PAW) method. The kinetic cutoff energy was set to 400 eV. The integration of the Brillouin zone is performed using a 2 × 2 × 1 Monkhorst–Pack grid. The geometries were optimized using a force-based conjugate-gradient method until the energy was converged to 1×10^{-5} eV per atom and the force to 0.05 eV $Å^{-1}$. The substrate structure of MoO_x was constructed by cutting the bulk MoO_3 along the c direction normal to the surface to avoid periodic interactions with a vacuum layer having a thickness of 15 Å. Subsequently, Pt clusters were placed on the surface of MoO_x to form the Pt/MoO_x-F model. To determine the activity of the as-constructed structures, the free energy diagrams were calculated as follows:

$$\Delta G = \Delta E + \Delta \text{ZPE} - T\Delta S$$

here ΔG and ΔE are the free energy change and the total energy change; ZPE, T, and S are the zero-point energy, temperature (298.15 K), and entropy, respectively. The free energy of $(H^+ + e)$ under standard conditions is determined as the half energy of H_2.

Results and discussion

Synthesis and characterization of Pt/MoO_x-F and its reference catalysts

The synthesis procedure of Pt/MoO_x-F is illustrated in Fig. 1. Specifically, the Pt cations were loaded on the mixed powder of MoO_3 and carbon black *via* a simple impregnation drying method to obtain the Pt precursor. The Pt precursor was then heated to a suitable temperature by the ultrafast flash joule heating method to obtain the Pt/MoO_x-F catalyst. The procedure involved subjecting the Pt precursor to a definite electrical voltage within 0.5 s in an argon environment, which makes the Pt precursor rapidly heat up to about 750 °C, and cool down to room temperature within the next 0.5 s, as shown in Fig. S4.† The entire heating process involves eight pulses, each pulse lasting 10 seconds, including 0.5 seconds of heating, 0.5 seconds of cooling, and about 9 seconds of waiting time. This synthesis process was used to construct a unique structure with fast electronic transport.

The crystal structure, morphology, and compositions of the as-prepared catalysts were investigated by different characterization techniques, as shown in Fig. 2. As illustrated in Fig. 2a,

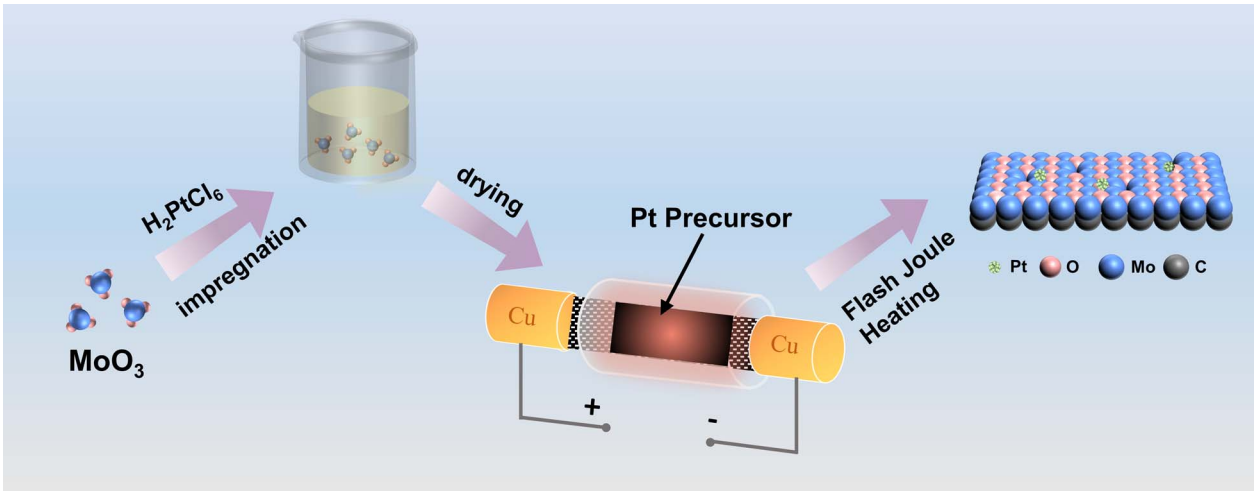

Fig. 1 Schematic illustration of the fabrication of Pt/MoO_x-F.

X-ray diffraction (XRD) patterns of MoO_x show two types of crystalline structures that could be assigned to the crystal phase of MoO_2 (JCPDS No. 65-5787) and MoO_3 (JCPDS No. 89-7112), respectively. After the introduction of Pt, Pt/MoO_x-F displays the same crystal structure as that of MoO_x. However, the XRD signal of metallic platinum is not observed in Pt/MoO_x-F, which could be related to the ultralow Pt loading (1.853 wt%) in the catalyst according to the inductively coupled plasma-atomic emission spectroscopy (ICP-AES) result (Table S2†). The morphology characterization studies of MoO_x and Pt/MoO_x-F were further performed by transmission electron microscopy (TEM). Despite the introduction of Pt, the TEM image of Pt/MoO_x-F (Fig. 2b) shows a morphology similar to that of MoO_x (Fig. S5†), but the size of the metal particles after Pt loading is significantly reduced, which is attributed to the unique interaction between Pt and the support. As depicted in Fig. 2b, the nanoparticles are approximately 7 nm in size (Fig. S5†) and are uniformly dispersed.

Moreover, insights into the microstructural characteristics of the optimal catalyst Pt/MoO_x-F, were obtained through High-Resolution Transmission Electron Microscopy (HR-TEM). We compared pure-phase MoO_2, MoO_3, and the Pt-free support MoO_x as control samples against the catalyst Pt/MoO_x-F. Fig. 2e and f show the HR-TEM images of pure phase MoO_3 and MoO_2, and the d-spacing values of $d = 0.326$ nm and $d = 0.286$ nm align with the (210) plane of MoO_3 and the (−102) plane of MoO_2, respectively. The HR-TEM image (Fig. 2d) of the MoO_x support reveals crystal plane spacings of 0.386 nm and 0.247 nm, corresponding to the (101) plane of MoO_3 and the (−211) plane of MoO_2, respectively. The combination of XRD and TEM shows that the structure of MoO_x is different from that of pure phase MoO_2 and MoO_3, which is heterogeneous and formed by MoO_2 and MoO_3. Similarly, the HR-TEM image of Pt/MoO_x-F (Fig. 2c) also shows the crystal planes of MoO_2 and MoO_3, (011) (crystal plane spacings: 0.345 nm) and (101) (crystal plane spacings: 0.387 nm), respectively, indicating that the heterogeneous MoO_x substrate is successfully synthesized despite the introduction of Pt. In addition, a third plane spacing of 0.226 nm is found in Pt/MoO_x-F, which is attributed to the (111) plane of Pt, indicating that Pt has been successfully loaded on the MoO_x substrate. The elemental mapping images illustrated in Fig. 2g elucidate the homogeneous distribution of C, O, Mo, and Pt within the Pt/MoO_x-F catalyst. Therefore, the experiments confirm that the structure of Pt/MoO_x-F consists of Pt nanoparticles loaded on the heterogeneous MoO_x-F substrate. According to previous reports,[31–34] the presence of heterogeneous structures might tend to increase the number of active sites, facilitate charge transfer, and accelerate mass diffusion.

The metal–support interaction between Pt sites and the MoO_x substrate was investigated by X-ray photoelectron spectroscopy and X-ray absorption spectroscopy measurements. To explore this interaction clearly, we prepared the Pt nanoparticle catalyst without MoO_x (Pt NPs) for comparative analysis. The white line peak intensity of X-ray absorption near edge structure (XANES) spectrum is highly correlated with the spatial structure and symmetry of the material,[13] so a series of Pt samples exhibit different white line peak intensities as shown in Fig. 3a. Specifically, the white line peak intensity of Pt NPs is higher than that of Pt foil, indicating the oxidized valence state of Pt in Pt NPs. However, after incorporating MoO_x, the white line peak intensity for Pt/MoO_x-F is observed to be lower than that of the Pt NPs and almost coincided with that of Pt foil, indicating a reduced oxidation state of Pt in Pt/MoO_x-F compared to the Pt NPs.

The detailed coordination environments of Pt were investigated by extended X-ray absorption fine structure (EXAFS). In the Pt L_3-edge EXAFS spectra (Fig. 3b), two prominent peaks are exhibited at about 1.6 Å and 2.7 Å for Pt/MoO_x-F and Pt NPs, which are ascribed to the first-shell Pt–O coordination and second-shell Pt–Pt/Mo coordination, respectively.[35–39] To determine the coordination type and obtain quantitative information on the coordination number, EXAFS fitting was performed. The results, as shown in Fig. S6 and Table S3,† indicate that the first-

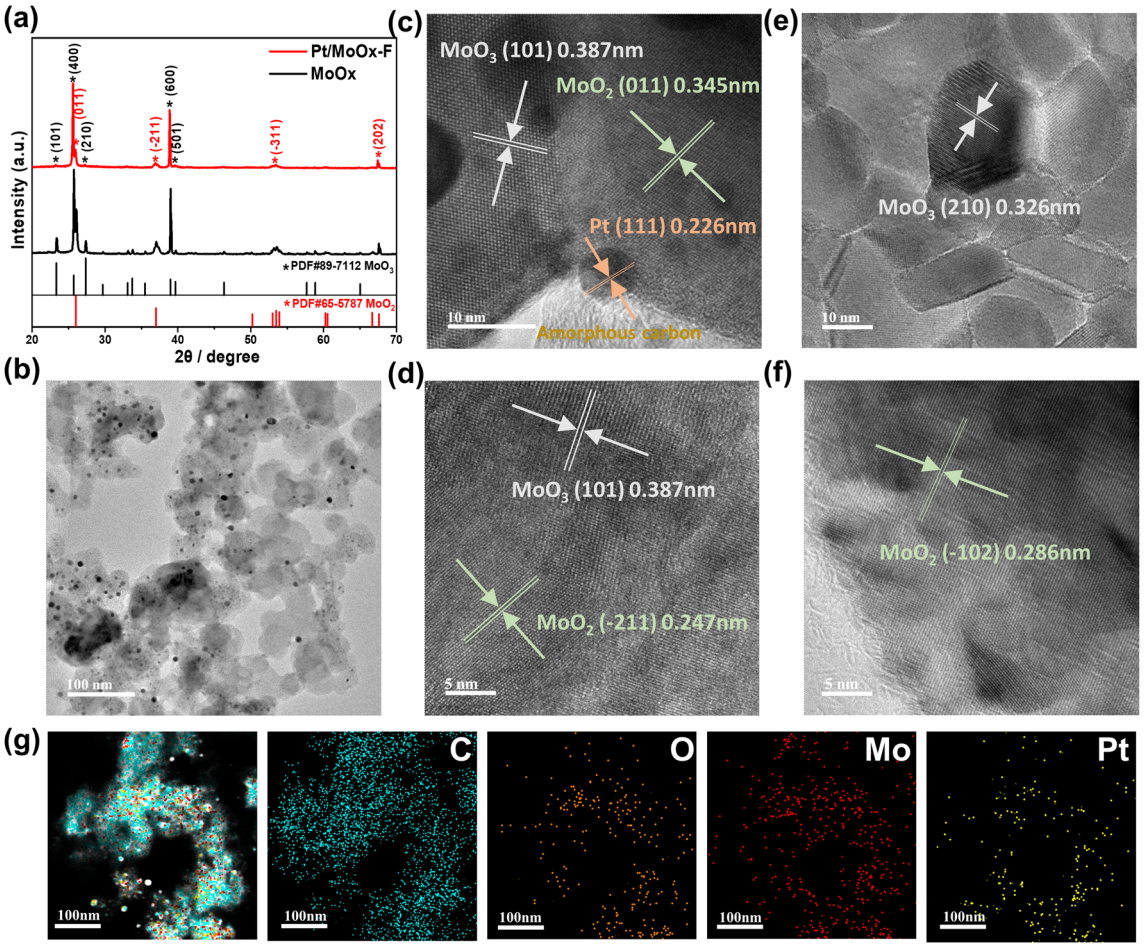

Fig. 2 Morphological and structural characterization: (a) XRD patterns of as-prepared Pt/MoO_x-F and MoO_x. (b) TEM image of Pt/MoO_x-F. HRTEM image of (c) Pt/MoO_x-F, (d) MoO_x, (e) MoO_3 and (f) MoO_2. (g) The elemental mapping images of Pt/MoO_x-F.

shell coordination of Pt/MoO_x-F is determined to be Pt–O bonding, and the second-shell coordination is Pt–Pt bonding and Pt–Mo bonding. For Pt NPs, the first-shell coordination is also determined to be Pt–O bonding, but the second-shell coordination is only Pt–Pt bonding. Additionally, it is noteworthy that the Pt NP sample has a lower Pt–Pt coordination number (CN) and a higher Pt–O CN than the Pt/MoO_x-F sample, which indicates the oxidation state of Pt in Pt NPs. The lower Pt–Pt CN in the Pt/MoO_x-F sample relative to Pt foil may result from an increased proportion of surface Pt sites due to their nanosize.[38]

Subsequently, we employed XPS to investigate the electronic state of Pt in Pt/MoO_x-F. As illustrated in Fig. 3c, the Pt 4f XPS spectrum of Pt NPs exhibits two peaks which are located at 72.23 eV and 75.53 eV. However, the Pt 4f XPS spectrum for Pt/MoO_x-F is located at a binding energy of 71.65 eV and 74.95 eV, and exhibits a shift toward a lower binding energy by approximately 0.58 eV relative to that of Pt NPs, indicating the lower valence state of Pt in Pt/MoO_x-F, which corresponds to the higher white line intensity of Pt NPs in XANES. The above analysis of the Pt valence state shows that the valence state of Pt decreases in the presence of the MoO_x substrate, which reveals the strong interaction between Pt and the MoO_x substrate.

Furthermore, we explored the valence states of Mo in the samples. The Mo 3d XPS spectrum of substrate MoO_x (Fig. 3d) exhibits three sets of peaks which can be ascribed to the oxidation states of Mo^{4+} (binding energy at 229.25 eV and 232.38 eV), Mo^{5+} (231.41 eV and, 234.54 eV), and Mo^{6+} (232.71 eV and 235.84 eV), respectively (Table S4†). The calculated area ratios for Mo^{4+} : Mo^{5+} : Mo^{6+} are about 1 : 2.33 : 7.21 (9.5% : 22.1% : 68.4%). After Pt loading, only two sets of peaks appeared in the Pt/MoO_x-F catalyst, corresponding to the oxidation states Mo^{5+} and Mo^{6+}. The area ratio of Mo^{5+} and Mo^{6+} is 25.4%:74.6%. It is noticeable that Mo^{4+} disappears after Pt loading and the ratio of Mo^{5+} and Mo^{6+} has increased compared to that of the MoO_x substrate. The above Mo 3d XPS analyses indicate that the introduction of Pt leads to the increase of the Mo valence state, which is further confirmed by the positive shift of the Mo L_3-edge absorption spectrum (Fig. 3e) of Pt/MoO_x-F compared to that of MoO_x.[40–43] Hence, we speculate that in the Pt/MoO_x-F catalyst, the Mo atoms transfer their electrons to the Pt atoms.

To deeply reveal the underlying electronic modulation mechanism within the Pt/MoO_x-F catalyst, we compared the work function (Φ) of MoO_x and Pt. The work function represents the minimum energy needed for an electron to transition from

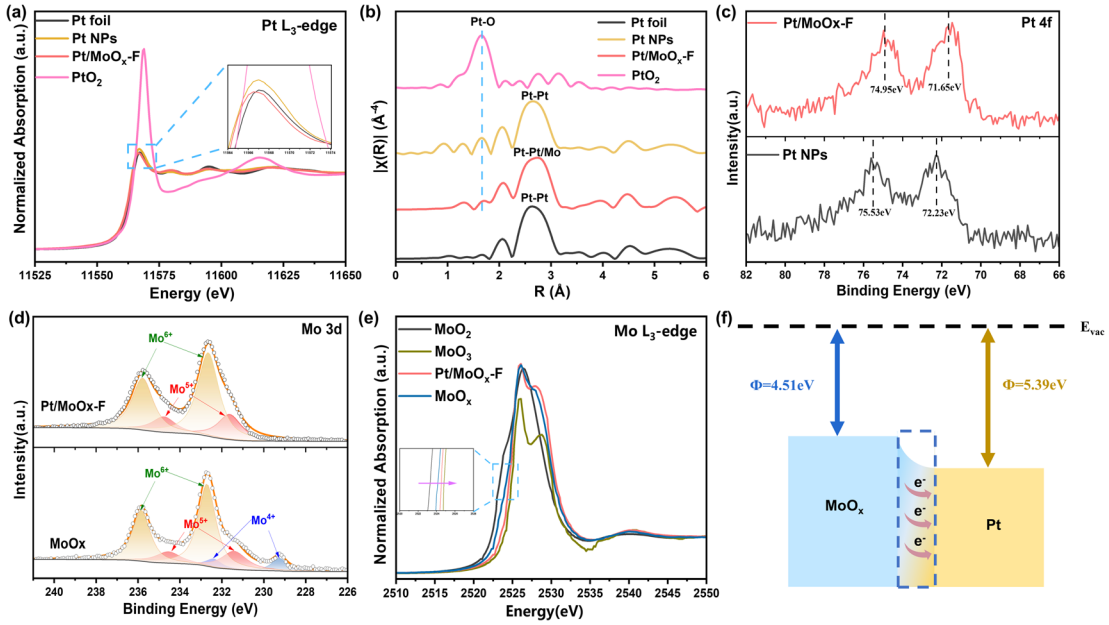

Fig. 3 Electronic structure characterization of Pt/MoO_x-F and reference samples. (a) The Pt L_3-edge XANES spectra. (b) The EXAFS curves of the Pt L_3-edge of Pt/MoO_x-F and reference catalysts. (c) Pt 4f XPS spectra of Pt/MoO_x-F with its reference sample Pt NPs. (d) Mo 3d XPS spectra of substrate MoO_x and catalyst Pt/MoO_x-F. (e) Mo L_3-edge XANES spectra. (f) Schematic work function diagram for Pt/MoO_x-F.

the Fermi level to the vacuum level. This indicator, Φ, implies electron escape ability and determines both the direction and possibility of electron transfer at the heterostructure interface.[44,45] As illustrated in Fig. S7,† the spectrum from the cut-off region reveals a work function for MoO_x of 4.51 eV, which is notably lower than the value previously documented for Pt (5.39 eV).[46] As illustrated in Fig. 3f, the work function value of Pt is larger than that of MoO_x, which reveals the formation of a Pt/MoO_x-F heterojunction which induces electron transfer from the lower work function region of the MoO_x substrate to the higher work function region of the Pt surface. The above results corroborate the metal–support electronic interaction between the MoO_x substrate and Pt nanoparticles in the Pt/MoO_x-F catalyst, leading to spatial charge redistribution. Recent studies also revealed that high-valence metal ions can optimize the electronic configuration of active sites.[47] Therefore, we suppose that in our Pt/MoO_x-F catalyst, the high valent Mo ions effectively regulate the electronic structure of Pt so that the electrons are transferred from Mo to Pt, which is conducive to the efficient catalysis of the HER.

HER performance of Pt/MoO_x-F and its reference catalysts

To corroborate the enhanced catalytic dynamics resulting from the synergistic interplay between Pt sites and the MoO_x substrate, we further evaluated the HER performance of the optimal Pt/MoO_x-F catalyst with control samples using a standard three-electrode system in an acidic electrolyte. Remarkably, Pt/MoO_x-F demonstrates superior activity in comparison to other reference samples. As depicted in the linear sweep voltammetry (LSV) curve (Fig. 4a), a notably low overpotential of merely 19.32 mV and 55.08 mV is necessary for Pt/MoO_x-F to achieve current densities of 10 mA cm^{-2} and 100 mA cm^{-2}, respectively. These values are exceedingly lower than those observed for the commercial 20 wt% Pt/C catalyst, which required 20.06 mV and 116.73 mV, respectively, and are also more favorable than the overpotentials recorded for other as-prepared samples (Fig. S8†). Furthermore, the mass activity of Pt/MoO_x-F reaches a remarkable 13.80 A mg_{Pt}^{-1} at an overpotential of 50 mV, which is an astounding 25-fold enhancement over that of the commercial 20 wt% Pt/C catalyst, whose mass activity stands at 0.56 A mg_{Pt}^{-1} (Fig. 4b and S9†). Therefore, Pt/MoO_x-F has distinctly enhanced catalytic activity and intrinsic performance compared to other as-prepared samples.

As another important descriptor of electrocatalytic performance, the corresponding Tafel slopes of all catalysts are plotted in Fig. 4c. Among all as-prepared catalysts, Pt/MoO_x-F exhibits the lowest Tafel slope of 19.94 mV dec^{-1}, superior to 20 wt% Pt/C (36.86 mV dec^{-1}), Pt/MoO_x-P (63.15 mV dec^{-1}), and Pt NPs (125.46 mV dec^{-1}), indicating the fastest reaction kinetics.[59–61] Additionally, Pt/MoO_x-F exhibits exceptional stability. As evidenced in Fig. 4d, during a constant-current electrolysis test conducted at 50 mA cm^{-2} for 15 hours, the voltage of Pt/MoO_x-F displayed minimal decay, whereas the commercial 20 wt% Pt/C catalyst showed significant voltage attenuation. As shown in Fig. S10,† Pt/MoO_x-F also showed negligible current attenuation during a 22-hour constant potential stability test, while the current density of the commercial 20 wt% Pt/C catalyst decreased from 10 mA cm^{-2} to about 0 mA cm^{-2}. Besides, we explored the structural stability of Pt/MoO_x-F by the TEM method, as shown in Fig. S11.† TEM images show that Pt/MoO_x-F retained the morphology and particle size of the parent phase, along with the lattice spacing. The mapping of post-HER indicates that Mo, O, and C elements

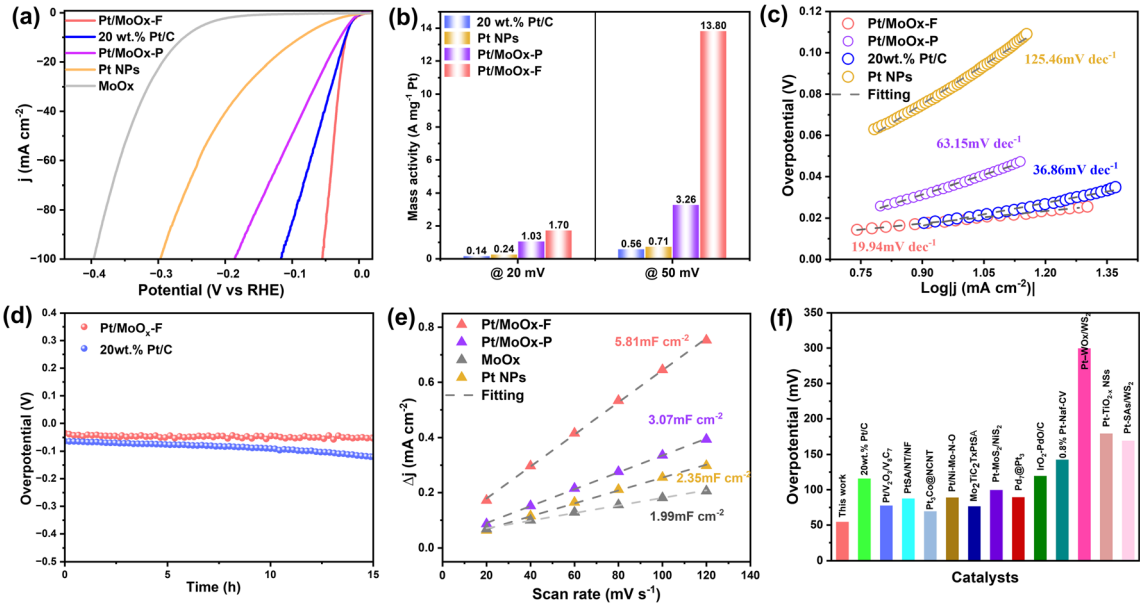

Fig. 4 Electrochemical HER performance in acidic electrolyte. (a) Polarization curves of Pt/MoO_x-F in comparison with 20 wt% Pt/C and other reference samples. (b) Mass activity at $\eta = 20$ mV and $\eta = 50$ mV of as-prepared samples. (c) Tafel plots for Pt/MoO_x-F and other reference samples. (d) Plot of overpotential *versus* time for Pt/MoO_x-F at a constant current density of 50 mA cm^{-2}. (e) Capacitive currents as a function of the scan rate of as-prepared samples. (f) In 0.5 M H_2SO_4 solution, comparison of the overpotentials at 100 mA cm^{-2} with the references. Data obtained from ref. 48–58 and references therein.

are distributed homogeneously with a slight aggregation of the Pt element. The above results jointly confirm the favorable stability of Pt/MoO_x-F in the hydrogen evolution reaction.

To delve deeper into the charge-transfer processes of catalysts, electrochemical impedance spectroscopy (EIS) was conducted. It is clear from the Nyquist plot presented in Fig. S12† that Pt/MoO_x-F exhibits the smallest semicircle radius compared to the other reference samples, indicating its heightened efficiency in facilitating electron transfer, which is beneficial for boosting HER performance. The electrochemical double-layer capacitance (C_{dl}) serves as an important indicator of the electrocatalysts' activity, given its direct proportionality to the electrochemical active surface area (ECSA). Utilizing C_{dl} parameters can offer additional insight into the intrinsic electroactivity of an electrocatalyst. Impressively, as demonstrated in Fig. 4e and S13,† the C_{dl} value for Pt/MoO_x-F registers at 5.81 mF cm^{-2}, surpassing that of MoO_x-F, Pt NPs and Pt/MoO_x-P. This suggests that the Pt/MoO_x-F sample has a substantially enhanced active surface area, which potentially translates to greater catalytic efficiency. Moreover, it also illustrates that Pt/MoO_x-F has plentiful active sites owing to the interaction between Pt and the substrate.[14]

When compared to recent studies on Pt-based electrocatalysts for the HER, Pt/MoO_x-F stands out as one of the top catalysts due to its low overpotential (Fig. 4f), high mass activity (Table S5†), and favorable Tafel slope (Fig. S14†). Additionally, the Pt/MoO_x-F catalyst also has excellent mass activity in alkaline HER (1 M KOH). As shown in Fig. S15,† the mass activity of Pt/MoO_x-F at $\eta = 150$ mV is 8.4 A mg_{Pt}^{-1}, which is approximately 7.3 times greater than that of 20 wt% Pt/C (1.15 A mg_{Pt}^{-1}). Hence, the above results verify that the strategy of loading Pt on the heterogeneous MoO_x substrate could significantly improve the electrochemical performance in the HER by optimizing the electronic structure of active sites.

To study the catalytic role of the heterogeneous MoO_x substrate in driving the hydrogen evolution reaction, we prepared samples with the same platinum loading onto pure-phase MoO_2 and MoO_3. The crystalline phase of the corresponding samples was confirmed by XRD as shown in Fig. S16.† Additionally, we tested the morphology and element distribution of the samples by TEM measurement. Fig. S17† shows the TEM images and corresponding size distribution diagram of the Pt/MoO_3, Pt/MoO_x-F, and Pt/MoO_2 samples, which indicate similar morphology and consistent nanoparticle sizes with each other. Fig. S18† shows the homogeneous distribution of C, O, Mo, and Pt elements in the three samples. Subsequently, we investigated the electronic structure of Pt/MoO_3 and Pt/MoO_2 samples by XPS and XAS.

Fig. 5a depicts the Mo 3d XPS spectra both before and after Pt loading of as-prepared samples. Notably, in the Pt/MoO_3 sample, the Mo-related peaks show no substantial shift following the introduction of platinum. Additionally, compared with MoO_3, the absorption edge of Pt/MoO_3 is almost not shifted, suggesting negligible interaction between Pt and the MoO_3 support. Conversely, upon Pt loading on the MoO_2 substrate, an apparent transformation in the Mo 3d XPS spectral profile is observed; the characteristic triplet peaks of MoO_2 transformed into a doublet. Specifically, the peak located at a binding energy of 229.25 eV vanishes, whilst the remaining peaks at 231.4 and 234.7 eV experience an obvious migration to higher binding energies. This indicates that the introduction of platinum increases the Mo valence state in the Pt/MoO_2 sample. Similarly,

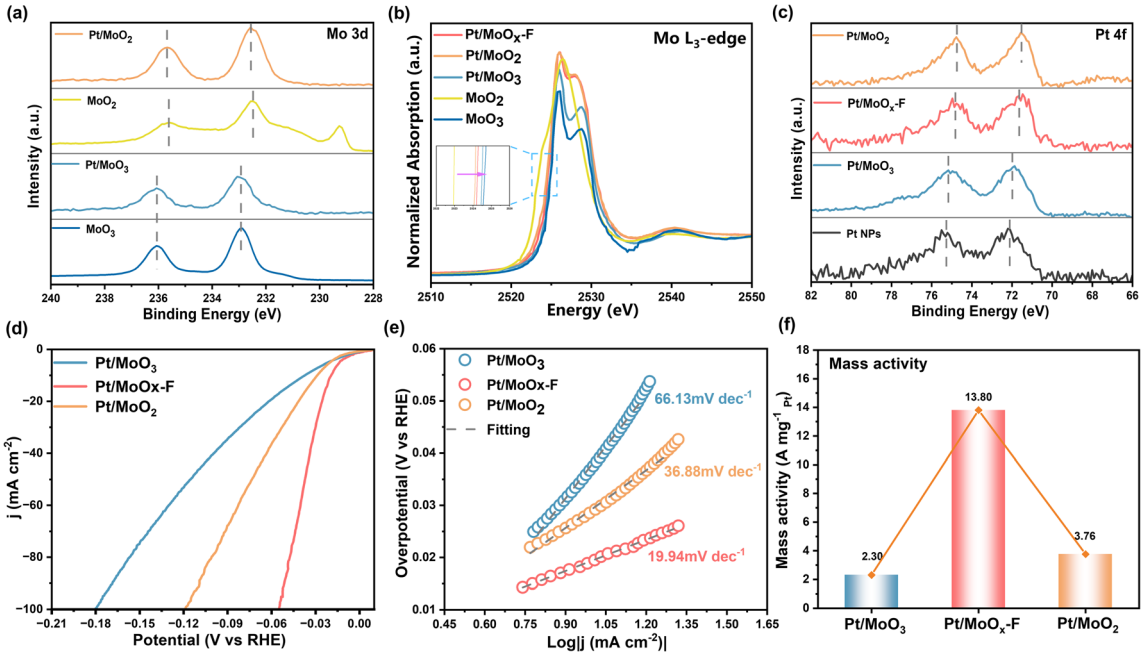

Fig. 5 Characterization of the electronic structures and assessment of the electrochemical HER performance for various substrates impregnated with platinum samples. (a) Mo 3d XPS spectra, (b) Mo L_3-edge XANES spectra, (c) Pt 4f XPS spectra, (d) polarization curves, (e) Tafel plots and (f) mass activity at $\eta = 50$ mV of Pt/MoO_x-F in comparison with other reference samples.

the absorption spectra observed at the Mo L_3-edge (Fig. 5b) corroborate the valence state shift trend that aligns with the findings presented in the Mo XPS 3d spectra. That is, compared with MoO_2, the Mo L_3-edge absorption spectrum of Pt/MoO_2 is positively shifted.

We further investigated the valence state of Pt, as shown in Fig. 5c. Observations reveal similar peak position of Pt between Pt NPs and Pt/MoO_3 samples, indicating hardly substantial changes in the Pt electronic structure in the presence of MoO_3. However, an evident shift towards lower binding energy is noted for the Pt peaks in both Pt/MoO_x-F and Pt/MoO_2 samples compared to those in the Pt NPs sample. This shift indicates that the valence states of Pt in Pt/MoO_x-F and Pt/MoO_2 samples are lower than those in Pt NPs. Combining the changes in the Mo valence state, it can be seen that the loading of Pt on MoO_3 leads to almost no metal–support interaction, whereas when loaded on MoO_x or MoO_2, there is tangible metal–support interaction. This might be the reason why the catalytic activities of Pt/MoO_2 and Pt/MoO_x-F are higher than that of Pt/MoO_3 as illustrated in Fig. 5d.

Fig. 5d presents the polarization curves of the studied samples. Notably, Pt/MoO_x-F demonstrates superior performance, evidenced by considerably reduced overpotentials when compared to both Pt/MoO_2 and Pt/MoO_3 at current densities of 10 and 100 mA cm^{-2} (Fig. S19†). Additionally, electrochemical impedance spectroscopy tests (Fig. S20†) have shown that the radius of the high-frequency semicircle for Pt/MoO_x-F is significantly smaller than that of Pt/MoO_2 and Pt/MoO_3 samples, indicating a substantial increase in conductivity and faster reaction kinetics in the presence of the MoO_x substrate. This indicates that among these three samples, Pt/MoO_x-F has the highest efficiency in charge transfer capability which is beneficial to the catalytic performance. The combination of spectroscopic and performance evaluation results confirms that the heterogeneous substrate MoO_x has an efficient charge transport capability and its strong interaction with Pt improves the charge distribution at the interface, which might be favorable to the enhancement of the HER activity.

Additionally, the Tafel slope of Pt/MoO_x-F, as depicted in Fig. 5e, is much lower in comparison to those recorded for Pt/MoO_2 (36.88 mV dec^{-1}) and Pt/MoO_3 (66.13 mV dec^{-1}). This indicates a faster kinetic process for the hydrogen evolution reaction at the Pt/MoO_x-F interface. Furthermore, Fig. 5f illustrates that the mass activities of the three catalysts display a distinct volcano plot trend. Among the three catalysts, Pt/MoO_x-F stands out with the highest mass activity, surpassing that of Pt/MoO_2 and Pt/MoO_3 by factors of 3.67 and 6 respectively, which underscores the superior catalytic performance of Pt/MoO_x-F for the hydrogen evolution reaction. The above findings highlight the enhanced conductivity and accelerated electron transfer kinetics at the heterogeneous Pt/MoO_x-F interface compared to the pure phase supported Pt sample, which indicates that the unique structure of Pt/MoO_x-F is conducive to enhancing HER activity.

Theoretical discussion

The density functional theory (DFT) calculations were performed to understand the mechanism of the excellent HER activity in Pt/MoO_x-F. According to the results obtained from XRD, TEM, and XPS, the MoO_x-F substrate was constructed using orthorhombic MoO_3 with several oxygen vacancies (O_v) to simulate the substrate with less oxygen. The heterostructure Pt/

MoO_x-F interface model was further constructed with Pt clusters on the MoO_x-F support, as shown in Fig. 6a and S21,† to approximate the actual structure. Charge density difference analysis of Pt/MoO_x-F shows that electrons were accumulated at the Pt sites and depleted in the MoO_x-F support (Fig. 6b), which aligns with the experimental results of XPS and XAS and verifies the electronic structure modulation.

To research the optimal HER catalytically active sites, we selected three sites of the Pt/MoO_x-F model (Fig. S22†), which are the Pt atom at the top of the Pt nanoparticles (marked as 1H), the Pt atom at the interface between the Pt and MoO_x-F substrate (marked as 2H) and the site at the MoO_x-F substrate (marked as 3H). The free energy ΔG_{H^*} of atomic hydrogen (H*) adsorbed on the surface of the catalyst can be considered a crucial physical quantity for evaluating the acidic HER activity of the catalyst.[62,63] The calculated energy diagram in Fig. 6c showed that ΔG_{H^*} on the 2H* sites of Pt/MoO_x-F is −0.02 eV, a value that is close to 0. In contrast, the top side of the Pt clusters has a negative ΔG_{H^*} (−0.05 eV), suggesting its comparatively strong binding to H*, which is unfavorable in the HER as it prevents the desorption of H*, while MoO_x shows a positive ΔG_{H^*} (0.09 eV), indicating that it needs extra energy to adsorb hydrogen, which is not conducive to the adsorption of H. According to the Sabatier principle, the most active catalytic site will have moderate hydrogen adsorption-free energy with $\Delta G_{H^*} \approx 0$.[64] Thus, the 2H site is the best hydrogen adsorption active site for the HER in Pt/MoO_x-F, which also confirms the key role of the charge transfer effect between the metal and support in the process of adsorption/desorption of reactants on active sites.

Additionally, based on the d-band center theory,[65] it is explicitly shown that the d-band center of Pt can be adjusted away from the Fermi level, to reduce the adsorption of H and further improve the HER activity. For comparison, we constructed Pt clusters (named Pt) as a model for Pt without a support (Fig. S21†). As illustrated in Fig. 6d, the d band center

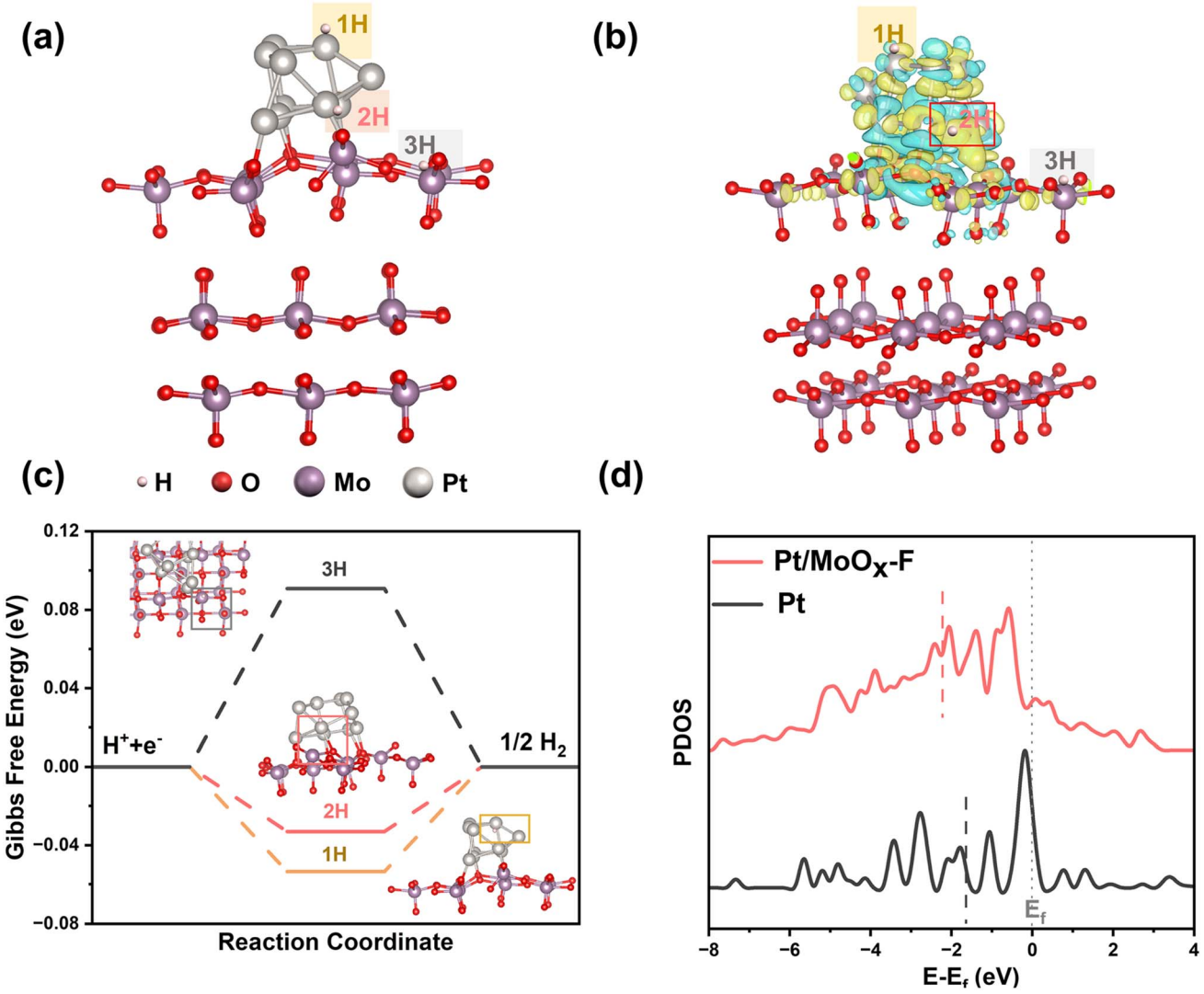

Fig. 6 First-principles calculations based on DFT. (a) Ball-stick models of Pt/MoO_x-F. (b) Charge density difference analysis of Pt/MoO_x-F; yellow and blue colors indicate electronic accumulation and depletion respectively. (c) H* adsorption Gibbs free energies and the corresponding equilibrium geometries of three different sites on Pt/MoO_x-F. (d) Density of electronic d states of Pt and Pt/MoO_x-F.

of Pt/MoO_x-F is noticeably negatively shifted with respect to the Fermi level compared to that of the sample Pt, suggesting the optimal absorption of hydrogen on the Pt of Pt/MoO_x-F. The DFT calculation therefore provides a connection between the electronic structure of Pt active site modulation and the improvement of HER performance. That is, the interaction between Pt and the MoO_x-F support induces the center of the Pt d band in Pt/MoO_x-F to negatively shift from the Fermi level, which weakens its interaction with H*, reduces the energy barrier in the H* desorption stage, and further accelerates the HER dynamics.

Conclusions

In summary, we have successfully devised a rapid and controllable ultrafast flash joule heating method within about a one-second heating timeframe to prepare Pt/MoO_x-F, which exhibited remarkable activity and stability for acidic HER. This method not only speeds up the synthesis process but also alleviates the problem of platinum aggregation, which is often caused by prolonged heat spots. Experimental evidence disclosed that Pt/MoO_x-F consists of platinum nanoparticles evenly distributed across the heterogeneous MoO_x substrate. Exhibiting a platinum content of merely 1.853 wt%, Pt/MoO_x-F demonstrates superior HER performance, characterized by a lower overpotential of 55.08 mV at a current density of 100 mA cm^{-2} and a more favorable Tafel slope of 19.94 mV dec^{-1}, outperforming the majority of previously reported Pt-based catalysts. The formation of the heterogeneous substrate significantly elevates catalyst conductivity, thereby facilitating swift electron transfer for HER processes. The interaction between Pt and the MoO_x support which is confirmed by XPS and XAS indicates that the formation of Pt–O and Pt–Mo bonds reduces particle agglomeration and bolsters catalytic endurance. Moreover, theoretical calculations confirm the strong metal–support interaction between Pt and the MoO_x support, which regulates the center of the Pt d-band negatively shifting from the Fermi energy level and reduces the adsorption of H*, thus accelerating the reaction kinetics and enhancing the catalytic activity. This work underscores the great potential of the ultrafast flash joule heating method for the preparation of highly efficient heterogeneous electrocatalysts and provides some new insights into the strategies for the regulation of metal–support interactions, thus paving the way for the development of highly efficient heterogeneous electrocatalysts.

Data availability

The data supporting this article have been included as part of the ESI.†

Author contributions

Lijuan Zhu: data curation, formal analysis, conceptualization, investigation, writing – original draft, writing – review & editing. Zhongjie Lai: investigation, methodology, formal analysis, validation. Jilong Xu: data curation, formal analysis, validation. Peiyu Ma: validation, writing – review & editing. Jaixiang Lu: investigation. Qian Xu, Lei Zheng, Lihui Wu: resources. Yitao Lin: formal analysis. Honghe Ding: resources, formal analysis. Jiawei Ge: software, methodology, formal analysis, writing – review & editing. Yifan Ye: conceptualization, supervision, funding acquisition, validation, writing – review & editing.

Conflicts of interest

There are no conflicts to declare.

Acknowledgements

This work was supported by the National Key Research and Development Program of China under project numbers 2023YFA1508004 and 2023YFF0716104, which provided funding for this project. We acknowledge the support from the National Natural Science Foundation of China under project number 22172153. We are also thankful for the USTC Research Funds of the Double First-Class Initiative under project number YD2310002007 and the Innovation Team Cultivation Fund of USTC. We acknowledge the support from the CAS Project for Young Scientists in Basic Research under project number YSBR-051. We would like to thank the Beijing Synchrotron Radiation Facility Synchrotron (beamline 1W1B and 4B7A stations) for providing the XAFS testing and Hefei Synchrotron Radiation Facility, Catalysis and Surface Science Beamline (BL11U), for providing the XPS and UPS testing for this work. Additionally, we acknowledge the Supercomputing Center of the University of Science and Technology of China (USTC) for providing computational resources.

References

1 S. Chu and A. Majumdar, *Nature*, 2012, **488**, 294–303.
2 Y. Gong, J. Yao, P. Wang, Z. Li, H. Zhou and C. Xu, *Chem. Eng. J.*, 2022, **43**, 282–296.
3 J. A. Turner, *Science*, 2004, **305**, 972–974.
4 H. I. Karunadasa, C. J. Chang and J. R. Long, *Nature*, 2010, **464**, 1329–1333.
5 F. Mueller-Langer, E. Tzimas, M. Kaltschmitt and S. Peteves, *Int. J. Hydrogen Energy*, 2007, **32**, 3797–3810.
6 H. Jin, C. Guo, X. Liu, J. Liu, A. Vasileff, Y. Jiao, Y. Zheng and S.-Z. Qiao, *Chem. Rev.*, 2018, **118**, 6337–6408.
7 J. Zhu, L. Hu, P. Zhao, L. Y. S. Lee and K. Y. Wong, *Chem. Rev.*, 2020, **120**, 851–918.
8 S. Sultan, J. N. Tiwari, A. N. Singh, S. Zhumagali, M. Ha, C. W. Myung, P. Thangavel and K. S. Kim, *Adv. Energy Mater.*, 2019, **9**, 1900624.
9 X. Li, J. Yu, J. Jia, A. Wang, L. Zhao, T. Xiong, H. Liu and W. Zhou, *Nano Energy*, 2019, **62**, 127–135.
10 T. He, W. Wang, F. Shi, X. Yang, X. Li, J. Wu, Y. Y and M. J, *Nature*, 2021, **598**, 76–81.
11 Y. Shi, Z. Ma, Y. Xiao, Y. Yin, W. Huang, Z. Huang, Y. Zheng, F. Mu, R. Huang, G. Shi, Y. Sun, X. Xia and W. Chen, *Nat. Commun.*, 2021, **12**, 3021.

12 A. Bruix, J. Rodriguez, P. J. Ramirez, S. D. Senanayake, J. Evans, J. B. Park, D. Stacchiola, P. Liu, J. Hrbek and F. Illas, *J. Am. Chem. Soc.*, 2012, **134**, 8968–8974.
13 W. Wang, Y. Wu, Y. Lin, J. Yao, X. Wu, C. Wu, X. Zuo, Q. Yang, B. Ge, L. Yang, G. Li, S. Chou, W. Li and Y. Jiang, *Adv. Funct. Mater.*, 2022, **32**, 2108464.
14 A. Shan, X. Teng, Y. Zhang, P. Zhang, Y. Xu, C. Liu, H. Li, H. Ye and R. Wang, *Nano Energy*, 2022, **94**, 106913.
15 J. Bai, J. Shang, J. Mei, X. Wang, C. Zhang, H. Kandambrige, D.-C. Qi, T. Liao and Z. S, *ACS Energy Lett.*, 2023, **8**, 3868–3875.
16 P. Chen, W. Huang, K. Li, D. Feng and Y. Tong, *Catalysts*, 2022, **12**, 859.
17 J. He, J. Li, Z. Yu, S. Li, J. Yuan and J. Cai, *Environ. Sci. Pollut. Res.*, 2024, **31**, 1530–1542.
18 L. Peng, D. Zhang, Z. Ma, D. Chu, C. Cazorla, R. Amal and Z. Han, *Small Struct.*, 2023, **4**, 2300194.
19 A. V. Avani and E. I. Anila, *Int. J. Hydrogen Energy*, 2022, **47**, 20475–20493.
20 H. S. Kim, J. B. Cook, H. Lin, J. S. Ko, S. H. Tolbert, V. Ozolins and B. Dunn, *Nat. Mater.*, 2017, **16**, 454–460.
21 L. Huang, L. Zhao, Y. Zhang, Q. Zhang, H. Luo, X. Zhang, T. Tang, L. Gu and J. Song, *Adv. Energy Mater.*, 2018, **8**, 1–7.
22 F. Haque, A. Zavabeti, B. Y. Zhang, J. T. Li, R. S. Datta, Y. Yin, Y. Wang, N. Mahmood, N. Pillai, N. Syed, H. Khan, A. Jannat, N. Wang, N. Medhekar, K. Kalantar-zadeh and J. Z. Qu, *J. Mater. Chem. A*, 2019, **7**, 257–268.
23 B. Dong, Y. N. Zhou, J. C. Zhou, Y. Ma, N. Yu, R. N. Luan, Y. W. Dong and Y. M. Chai, *Fuel*, 2022, **324**, 124343.
24 F. Guo, T. J. Macdonald, A. J. Sobrido, L. Liu, J. Feng and G. He, *Adv. Sci*, 2023, **10**, 2301098.
25 H. Zhang, P. Song, P. Yao, D. Zhang, J. Cao, X. Gong, C. Han and W. Xu, *Chem. Eng. J.*, 2023, **470**, 144375.
26 J. Park, S. Lee, H. E. Kim, A. Cho, S. Kim, Y. Ye, J. W. Han, H. Lee, J. H. Jang and J. Lee, *Angew. Chem., Int. Ed.*, 2019, **58**, 16038–16042.
27 L. Xing, R. Liu, Z. Gong, J. Liu, J. Liu, H. Gong, K. Huang and H. Fei, *Nano Res.*, 2022, **15**, 3913–3919.
28 Y. Yao, Z. Huang, P. Xie, S. D. Lacey, R. J. Jacob, H. Xie, F. J. Chen, A. Nie, T. Pu, M. Rehwoldt, D. Yu, M. R. Zachariah, C. Wang, R. S. Yassar, J. Li and L. Hu, *Science*, 2018, **359**, 1489–1494.
29 B. Deng, Z. Wang, W. Chen, J. T. Li, D. X. Luong, R. A. Carter, G. Gao, B. Yakobson, Y. Zhao and J. M. Tour, *Nat. Commun.*, 2022, **13**, 262.
30 H. Niu, Q. Wang, C. Huang, M. Zhang, Y. Yan, T. Liu and W. Zhou, *Appl. Sci.*, 2023, **13**, 2177.
31 G. Q. Zhao, K. Rui, S. X. Dou and W. Sun, *Adv. Funct. Mater.*, 2018, **28**, 1803291.
32 D. Y. Wang, M. Gong, H.-L. Chou, C. J. Pan, H. A. Chen, Y. Wu, M. C. Lin, M. Guan, J. Yang, C. W. Chen, Y. L. Wang, B. J. Hwang, C. C. Chen and H. Dai, *J. Am. Chem. Soc.*, 2015, **137**(4), 1587–1592.
33 X. Zou, Y. Liu, G. D. Li, Y. Wu, D. P. Liu, H. W. Li, D. Wang, Y. Zhang and X. Zou, *Adv. Mater.*, 2017, **29**, 1700404.
34 S. Yin, W. Tu, Y. Sheng, Y. Du, M. Kraft, A. Borgna and R. Xu, *Adv. Mater.*, 2018, **30**, 1705106.
35 Y. Ren, Y. Tang, L. Zhang, X. Liu, L. Li, S. Miao, D. S. Su, A. Wang, J. Li and T. Zhang, *Nat. Commun.*, 2019, **10**, 4500.
36 Y. Zhao, P. V. Kumar, X. Tan, X. Lu, X. Zhu, J. Jiang, J. Pan, S. Xi, H. Y. Yang, Z. Ma, T. Wan, D. Chu, W. Jiang, S. C. Smith, R. Amal, Z. Han and X. Lu, *Nat. Commun.*, 2022, **13**, 2430.
37 Q. Yang, H. Liu, P. Yuan, Y. Jia, L. Zhuang, H. Zhang, X. Yan, G. Liu, Y. Zhao, J. Liu, S. Wei, L. Song, Q. Wu, B. Ge, L. Zhang, K. Wang, X. Wang, C. R. Chang and X. Yao, *J. Am. Chem. Soc.*, 2022, **144**, 2171–2178.
38 K. Zhang, W. Yang, C. Ma, Y. Wang, C. Sun, Y. Chen, P. Duchesne, J. Zhou, J. Wang, Y. Hu, M. N. Banis, P. Zhang, F. Li, J. Li and L. Chen, *NPG Asia Mater.*, 2015, **7**, e153.
39 Z. Li, Y. Xiao, P. R. Chowdhury, Z. Wu, T. Ma, J. Z. Chen, G. Wan, T. K. Kim, D. Jing, P. He, P. J. Potdar, L. Zhou, Z. Zeng, X. Ruan, J. T. Miller, J. P. Greeley, Y. Wu and A. Varma, *Nat. Catal.*, 2021, **4**, 882–891.
40 K. E. Lee, L. Liu and T. L. Kelly, *J. Phys. Chem. C*, 2014, **118**, 27735–27741.
41 T. Ressler, J. Wienold, R. Jentoft and T. Neisius, *J. Catal.*, 2002, **210**, 67–83.
42 S. P. Cramer, T. K. Eccles, F. W. Kutzler, K. O. Hodgson and L. E. Mortenson, *J. Am. Chem. Soc.*, 1976, **98**, 1287–1288.
43 J. Wong, R. P. Messmer and D. H. Maylotte, *Phys. Rev. B: Condens. Matter Mater. Phys.*, 1984, **30**, 5596–5610.
44 S. Hao, B. Yang and Y. Gao, *Phys. Status Solidi B*, 2017, **254**, 1600245.
45 X. Teng, Z. Wang, Y. Wu, Y. Zhang, B. Yuan, Y. Xu, R. Wang and A. Shan, *Nano Energy*, 2024, **122**, 109299.
46 R. Samanta, B. K. Manna, R. Trivedi, B. Chakraborty and S. Barman, *Chem. Sci.*, 2024, **15**, 364–378.
47 B. Zhang, L. Wang, Z. Cao, S. M. Kozlov, F. Pelayo Garcia de Arquer, C. T. Dinh, J. Li, Z. Wang, X. Zheng, L. Zhang, Y. Wen, O. Voznyy, R. Comin, P. D. Luna, W. Bi, E. ErcanAlp, C. Pao, L. Zheng, Y. Hu, Y. Ji, Y. Li, Y. Zhang, L. Cavallo, H. Peng and E. H. Sargent, *Nat. Catal.*, 2020, **3**, 985–992.
48 J. Zhang, Y. Zhao, X. Guo, C. Chen, C. Dong, C. T. Liu, C. Han, Y. Li, Y. Gogotsi and G. Wang, *Nat. Catal.*, 2018, **1**, 985–992.
49 L. Zhang, L. Han, H. Liu, X. Liu and J. Luo, *Angew. Chem., Int. Ed.*, 2017, **56**, 13694–13698.
50 S. Zhang, X. Lu, Z. Wu, D. Luan, X. Wen and D. Lou, *Angew. Chem., Int. Ed.*, 2021, **60**, 19068–19073.
51 W. Yu, Z. Chen, Y. Fu, W. Xiao, B. Dong, Y. Chai, Z. Wu and L. Wang, *Adv. Funct. Mater.*, 2023, **33**, 2210855.
52 Y. Guan, Y. Feng, J. Wan, X. Yang, L. Fang, X. Gu, R. Liu, Z. Huang, J. Li, J. Luo, C. Li and Y. Wang, *Small*, 2018, **14**, 1800697.
53 Y. Liu, N. Yodsin, T. Li, H. Wu, R. Jia, L. Shi, Z. Lai, S. Namuangruk and L. Huang, *Mater. Horiz.*, 2024, **11**, 1964–1974.
54 R. Samanta, R. Mishra, B. K. Manna and S. Barman, *Renewable Energy*, 2022, **191**, 151–160.
55 J. Yu, D. Wei, Z. Zheng, W. Yu, H. Shen, Y. Qu, S. Wen, Y. U. Kwon and Y. Zhao, *J. Colloid Interface Sci.*, 2020, **566**, 505–512.

56 L. S. Oh, J. Y. Kim, H. W. Kim, J. Han, E. Lim, W. B. Kim, J. H. Park and H. J. Kim, *Chem. Commun.*, 2021, **57**, 11165–11168.
57 K. M. Naik, E. Higuchi and H. Inoue, *Nanoscale*, 2020, **12**, 11055–11062.
58 Y. Li, Y. Sheng, L. Shao, Y. Li, W. Xu, S. Zhang, F. Shao and J. Wang, *J. Mater. Chem. A*, 2024, **12**, 8724–8733.
59 H. Zhang, L. Cao, Y. Wang, Z. Gan, F. Sun, M. Xiao, Y. Yang, B. Mei, D. Wu, J. Lu, H. He and Z. Jiang, *ACS Appl. Mater. Interfaces*, 2021, **13**, 47252–47261.
60 D. Liu, X. Li, S. Chen, H. Yan, C. Wang, C. Wu, Y. A. Haleem, S. Duan, J. Lu, B. Ge, P. M. Ajayan, Y. Luo, J. Jiang and L. Song, *Nat. Energy*, 2019, **4**, 512–518.
61 S. Khamgaonkar, M. Okasha and V. Maheshwari, *Inorg. Chem. Front.*, 2023, **10**, 6812–6848.
62 Y. Guo, T. Park, J. W. Yi, J. Henzie, J. Kim, Z. Wang, B. Jiang, Y. Bando, Y. Sugahara, J. Tang and Y. Yamauchi, *Adv. Mater.*, 2019, **31**, 1807134.
63 S. Shen, Z. Lin, K. Song, Z. Wang, L. Huang, L. Yan, F. Meng, Q. Zhang, L. Gu and W. Zhong, *Angew. Chem., Int. Ed.*, 2021, **60**, 12360–12365.
64 H. Ooka, J. Huang and K. S. Exner, *Front. Energy Res.*, 2021, **9**, 654460.
65 S. Jiao, X. Fu and H. Huang, *Adv. Funct. Mater.*, 2022, **32**, 2107651.